

Gravity waves and mesospheric clouds in the summer middle atmosphere: A comparison of lidar measurements and ray modeling of gravity waves over Sondrestrom, Greenland

Andrew J. Gerrard,¹ Timothy J. Kane,² Stephen D. Eckermann,³ and Jeffrey P. Thayer⁴

Received 23 July 2002; revised 13 February 2004; accepted 24 March 2004; published 22 May 2004.

[1] We conducted gravity wave ray-tracing experiments within an atmospheric region centered near the ARCLITE lidar system at Sondrestrom, Greenland (67°N, 310°E), in efforts to understand lidar observations of both upper stratospheric gravity wave activity and mesospheric clouds during August 1996 and the summer of 2001. The ray model was used to trace gravity waves through realistic three-dimensional daily-varying background atmospheres in the region, based on forecasts and analyses in the troposphere and stratosphere and climatologies higher up. Reverse ray tracing based on upper stratospheric lidar observations at Sondrestrom was also used to try to objectively identify wave source regions in the troposphere. A source spectrum specified by reverse ray tracing experiments in early August 1996 (when atmospheric flow patterns produced enhanced transmission of waves into the upper stratosphere) yielded model results throughout the remainder of August 1996 that agreed best with the lidar observations. The model also simulated increased vertical group propagation of waves between 40 km and 80 km due to intensifying mean easterlies, which allowed many of the gravity waves observed at 40 km over Sondrestrom to propagate quasi-vertically from 40–80 km and then interact with any mesospheric clouds at 80 km near Sondrestrom, supporting earlier experimentally-inferred correlations between upper stratospheric gravity wave activity and mesospheric cloud backscatter from Sondrestrom lidar observations. A pilot experiment of real-time runs with the model in 2001 using weather forecast data as a low-level background produced less agreement with lidar observations. We believe this is due to limitations in our specified tropospheric source spectrum, the use of climatological winds and temperatures in the upper stratosphere and mesosphere, and missing lidar data from important time periods. **INDEX TERMS:** 0320 Atmospheric Composition and Structure: Cloud physics and chemistry; 3334 Meteorology and Atmospheric Dynamics: Middle atmosphere dynamics (0341, 0342); 3349 Meteorology and Atmospheric Dynamics: Polar meteorology; 3364 Meteorology and Atmospheric Dynamics: Synoptic-scale meteorology; 3367 Meteorology and Atmospheric Dynamics: Theoretical modeling; **KEYWORDS:** gravity waves, lidar, mesospheric clouds

Citation: Gerrard, A. J., T. J. Kane, S. D. Eckermann, and J. P. Thayer (2004), Gravity waves and mesospheric clouds in the summer middle atmosphere: A comparison of lidar measurements and ray modeling of gravity waves over Sondrestrom, Greenland, *J. Geophys. Res.*, 109, D10103, doi:10.1029/2002JD002783.

1. Introduction

[2] Assessing the impact of gravity wave momentum deposition in the stratosphere and mesosphere is crucial for a better understanding of the global, middle atmospheric circulation [e.g., Holton and Alexander, 2000; Fritts and Alexander, 2003; and references therein]. General circula-

tion models (GCMs) using relatively large spatial grids with subgrid-scale gravity wave drag parameterizations have done a reasonable job of replicating the observed thermal and dynamical structure of the middle atmosphere [Pawson *et al.*, 2000]. However, finer-scale processes, including mechanisms of gravity wave breaking, wave-wave interactions, and critical-level interaction, are areas of ongoing research and have yet to be unambiguously resolved. Other areas of active research include localized gravity wave generation, daily variability, propagation mechanisms, and regional influence across different altitude levels; topics that can be grouped under the general topic of “synoptic-scale gravity wave activity.”

[3] Historically, issues involving synoptic gravity wave activity have focused on their global influences on middle atmospheric climate and have been addressed with simple

¹Kinard Laboratory, Clemson University, Clemson, South Carolina, USA.

²Pennsylvania State University, University Park, Pennsylvania, USA.

³Middle Atmospheric Dynamics Section, E. O. Hulburt Center for Space Research, Naval Research Laboratory, Washington, D. C., USA.

⁴Ionospheric and Space Physics Group, SRI International, Menlo Park, California, USA.

Report Documentation Page

Form Approved
OMB No. 0704-0188

Public reporting burden for the collection of information is estimated to average 1 hour per response, including the time for reviewing instructions, searching existing data sources, gathering and maintaining the data needed, and completing and reviewing the collection of information. Send comments regarding this burden estimate or any other aspect of this collection of information, including suggestions for reducing this burden, to Washington Headquarters Services, Directorate for Information Operations and Reports, 1215 Jefferson Davis Highway, Suite 1204, Arlington VA 22202-4302. Respondents should be aware that notwithstanding any other provision of law, no person shall be subject to a penalty for failing to comply with a collection of information if it does not display a currently valid OMB control number.

1. REPORT DATE 13 FEB 2004		2. REPORT TYPE		3. DATES COVERED 00-00-2004 to 00-00-2004	
4. TITLE AND SUBTITLE Gravity waves and mesospheric clouds in the summer middle atmosphere: A comparison of lidar measurements and ray modeling of gravity waves over Sondrestrom, Greenland				5a. CONTRACT NUMBER	
				5b. GRANT NUMBER	
				5c. PROGRAM ELEMENT NUMBER	
6. AUTHOR(S)				5d. PROJECT NUMBER	
				5e. TASK NUMBER	
				5f. WORK UNIT NUMBER	
7. PERFORMING ORGANIZATION NAME(S) AND ADDRESS(ES) Naval Research Laboratory, E.O. Hulburt Center for Space Research, Washington, DC, 20375				8. PERFORMING ORGANIZATION REPORT NUMBER	
9. SPONSORING/MONITORING AGENCY NAME(S) AND ADDRESS(ES)				10. SPONSOR/MONITOR'S ACRONYM(S)	
				11. SPONSOR/MONITOR'S REPORT NUMBER(S)	
12. DISTRIBUTION/AVAILABILITY STATEMENT Approved for public release; distribution unlimited					
13. SUPPLEMENTARY NOTES					
14. ABSTRACT					
15. SUBJECT TERMS					
16. SECURITY CLASSIFICATION OF:			17. LIMITATION OF ABSTRACT	18. NUMBER OF PAGES	19a. NAME OF RESPONSIBLE PERSON
a. REPORT unclassified	b. ABSTRACT unclassified	c. THIS PAGE unclassified			

global parameterizations of wave momentum flux divergence and turbulent diffusion due to waves from simplified or indistinct tropospheric sources [Fritts and Alexander, 2003; Kim *et al.*, 2003]. For example, many gravity wave drag parameterizations in general circulation models and climatological ray-tracing models include an intermittency factor that is tuned such that the resultant gravity wave momentum deposition replicates climatological characteristics [e.g., Alexander and Rosenlof, 2003]. On shorter timescales and within regional domains, however, these same gravity wave coupling processes should also affect the short-term regional evolution of the middle atmosphere. Regional mesoscale model simulations that resolve some gravity waves demonstrate this [e.g., Dörnbrack *et al.*, 1998; Horinouchi *et al.*, 2002], but it is difficult to extend these tools to run over larger domains and into the stratosphere and mesosphere.

[4] Research on synoptic gravity wave activity, including the forecasting of such activity in the middle and upper atmosphere, is rare due to a lack of both high-resolution synoptic measurements of this region (necessary for model verification) and adequate modeling efforts and techniques. Recent efforts to forecast middle atmospheric gravity waves have been motivated by an emerging understanding of their important role in forming high-altitude clouds. Polar stratospheric clouds (PSCs) form in winter and are important in ozone loss chemistry. In the Arctic, lower stratospheric gravity waves forced by flow over mountains (mountain waves) often drop temperatures in the ascent phases of the wave to the point where it is cold enough for these clouds to form. Thus, considerable effort has been devoted to forecast and model stratospheric mountain waves in the Arctic in support of various ozone-related measurement campaigns [e.g., Bacmeister *et al.*, 1994; Dörnbrack *et al.*, 1998, 2001; Dörnbrack and Leutbecher, 2001; Hertzog *et al.*, 2002; Pierce *et al.*, 2003].

[5] Gravity waves also appear to be important for the microphysics of high-altitude mesospheric clouds (MCs) observed in cold summer upper mesosphere [Jensen and Thomas, 1994; Rapp *et al.*, 2002]. MCs are also known as noctilucent clouds (NLCs) by ground-based observers or as polar mesospheric clouds (PMCs) by the atmospheric remote sensing community, although there are many reports of these clouds in non-polar environments [e.g., Thomas *et al.*, 1994; von Cossart *et al.*, 1996; Wickwar *et al.*, 2002]. Correlations between gravity waves impinging upon the mesosphere from below and MCs have been documented using molecular/aerosol lidar observations at the ARCTIC Lidar TEchnology (ARCLITE) facility at the Sondrestrom research site in Greenland (67°N, 310°E) [e.g., Gerrard *et al.*, 1998 (hereafter GKT98); Gerrard *et al.*, 2002a; Thayer *et al.*, 2003; Gerrard *et al.*, 2004]. These papers have been the first to show experimentally and statistically that enhancements of high frequency upper stratospheric gravity wave variance observed by molecular/aerosol lidar are associated with reductions in MC volume backscatter. Stated more colloquially, the higher the underlying stratospheric gravity wave activity, the more tenuous the mesospheric cloud.

[6] Gravity waves indirectly cool the summer mesosphere by driving a vigorous mean upwelling circulation through momentum deposition, a quasi-continuous processes that

maintains the cold synoptic conditions suitable for MC formation [e.g., Siskind *et al.*, 2003]. In addition, individual gravity wave fluctuations play a direct role in MC microphysics via particle sublimation [Rapp *et al.*, 2002]. Thus, gravity waves have a “dual nature” in controlling MC properties in the high latitude summer mesosphere. They indirectly control MC distributions on global spatial scales and weekly temporal scales through their breaking effects on the circulation, but also act to reduce MCs on regional spatial scales and over hourly temporal scales through their induced temperature oscillations. Such influences demonstrate the need for continued research into gravity wave generation and forecasting, especially from an MC modeling perspective.

[7] With these latter needs in mind, it is the purpose of this paper to model some of these gravity wave processes near Sondrestrom during summer and compare them with lidar observations. These tasks are accomplished by using the Gravity-wave Regional Or Global Ray Tracer (GROGRAT), a gravity wave ray-tracing model that is used here with daily tropospheric and stratospheric analyses as well as data from an empirical middle atmospheric model to simulate the amount of gravity wave activity over this high latitude region. These model-generated values are then compared to gravity wave activity measured from upper stratospheric relative atmospheric density perturbations that were obtained by the Sondrestrom lidar.

[8] In Section 2 of this paper we present background on the data resources used in this study. In Section 3 we discuss the ray-tracing model, specifically focusing on run parameters and the creation of a representative tropospheric gravity wave source spectrum using observationally constrained reverse ray tracing. In Section 4 we present the results of the 1996 model runs as compared to the lidar data. In Section 5 we present the results of the 2001 model runs as compared to lidar data. In Section 6 we discuss the implications of these results, and we summarize major findings and conclusions in the final section.

2. Data Resources

[9] This study used data from three primary sources. First, for the 1996 gravity wave experiments discussed in Section 4, daily (12 UT) background geopotential height and temperature fields in the troposphere and stratosphere were specified using National Centers for Environmental Prediction (NCEP) operational analyses from the Data Support Section of the Scientific Computing Division at the National Center for Atmospheric Research (DSS-SCD-NCAR). These fields were subsequently averaged onto $2.5^\circ \times 2.5^\circ$ latitude-longitude grids at 18 pressure levels, ranging from 1000 hPa to 0.4 hPa. Since no stratospheric data were available at 00 UT, we averaged the two adjacent 12 UT fields to obtain a data representation at all pressure levels for 00 UT. The mid-stratospheric analyses were compared to stratospheric analyses from the Stratospheric Research Group at the Free University of Berlin [e.g., Pawson and Naujokat, 1997; Labitzke and van Loon, 1999]; similar results were noted. For the gravity wave model experiments during 2001 discussed in Section 5, we used data from the NCEP Aviation Model (AVN) forecasts. The AVN model was

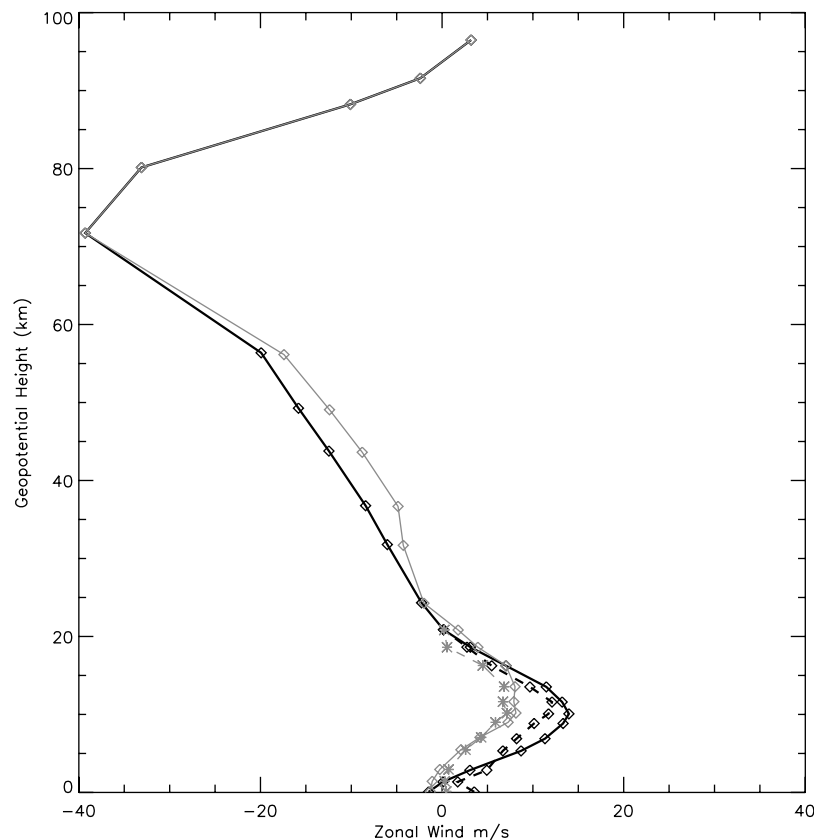


Figure 1. Computed geostrophic zonal wind profiles over Sondrestrom, Greenland on the 6th (solid black line) and the 11th (solid gray line) of August 1996. Dashed lines represent corresponding analysis winds. Diamonds represent sampling altitudes. Note that NCEP analysis winds abate above ~ 20 km. Data values above ~ 55 km were obtained from the CIRA-86 model.

combined in late 2002 with the Medium Range Forecast (MRF) model and collectively called the Global Forecast System (GFS). These operational analyses are based on data from the early 00 UT radiosonde-satellite reports and are used to initialize atmospheric forecasts from the AVN global model. The original $1^\circ \times 1^\circ$ data were rebinned to $2.5^\circ \times 2.5^\circ$ so as to be consistent with analysis fields used for the 1996 model configuration.

[10] The geopotential height fields were used to calculate geostrophic winds at all altitudes. Upper tropospheric and stratospheric winds were calculated following *Randel* [1987], while lower tropospheric winds were processed in a more conventional manner (e.g., no truncation of 6th or higher-order spherical harmonics). These geostrophic winds were compared to NCEP analysis winds throughout the troposphere. A sample comparison of zonal winds from 0–20 km over Sondrestrom on August 6th, 1996 and August 11th, 1996 is given in Figure 1, showing general agreement (winds at higher altitudes are discussed shortly). Geostrophic winds were used throughout this study for a variety of reasons, the chief being the desire to avoid having to smoothly splice station winds at 20 km with geostrophic winds at 25 km. If done poorly, large shears can arise at ~ 20 – 25 km which could spuriously remove gravity waves via WKB violations. The NCEP temperature profiles over Sondrestrom were also compared to experimentally obtained temperatures obtained with the ARCLITE lidar

system [*Gerrard et al.*, 2002b] and were shown to agree reasonably well.

[11] The second data resource was the Committee on Space Research (COSPAR) International Reference Atmosphere (hereafter CIRA-86) [*Fleming et al.*, 1990], which is based on the same data set as the Extended Mass Spectrometer and Incoherent Scatter Empirical Model (MSISE-90) [*Hedin*, 1991]. CIRA-86 fields provided temperature, geopotential height, and zonal wind for altitudes above the uppermost altitudes of the NCEP data (i.e., above 0.4 hPa ≈ 55 km for 1996 runs and above 10 hPa ≈ 32 km for 2001 runs). CIRA-86 provides zonal winds only. Thus, upper-level meridional winds were smoothly extrapolated upwards from the uppermost NCEP meridional wind value by progressively relaxing with increasing altitude to a constant value of -2 ms^{-1} (i.e., directed north to south), which is broadly representative of mean summertime meridional winds at mesospheric altitudes [e.g., *Kishore et al.*, 2003]. These empirical upper-level CIRA-86 data were held constant over each of the model days. In the absence of gravity waves, the thermal structure of the high latitude upper stratosphere and lower- to mid-mesosphere is relatively undisturbed during mid-summer [e.g., *Lübken*, 1999; *Gerrard et al.*, 2000]. Use of invariant upper-level winds is also reasonable since there is little tidal activity [e.g., *Hagan and Forbes*, 2002, 2003] or short-term planetary wave influence during summer at these altitudes. When all these

data were combined, the model atmospheric background consisted of winds, temperature, and geopotential heights at 23 different pressure levels (1000.0, 850.0, 700.0, 500.0, 400.0, 300.0, 250.0, 200.0, 150.0, 100.0, 70.0, 50.0, 30.0, 10.0, 5.0, 2.0, 1.0, 0.4, 0.046, 0.0103, $1.78\text{e-}3$, $8.42\text{e-}4$, $3.1\text{e-}4$ hPa), spanning the height range ~ 0 –105 km. Sample upper-level zonal wind profiles from ~ 0 –95 km using this combination of NCEP and CIRA-86 data are plotted in Figure 1.

[12] The most difficult aspect of the model simulations involves devising a method for specifying a broadly representative source spectrum of gravity waves in the troposphere, since tropospheric sources for middle atmospheric gravity waves remain highly uncertain, particularly in the summer extratropics [Fritts and Alexander, 2003]. To provide some observational constraints on this problem, we used (as our third data resource) stratospheric gravity wave observations from the ARCLITE molecular/aerosol lidar system located at Sondrestrom, Greenland [Thayer et al., 1995; Thayer et al., 1997]. Upper stratospheric gravity wave activity from the lidar is derived by time-averaging root-mean square (RMS) relative density perturbations using a sliding two-hour window, much like the procedures used by Senft and Gardner [1991] (see GKT98 and Gerrard et al. [2004] for further details). This method resolves waves with ground-based temporal periods $T = 2\pi/|\Omega|$ between 30 minutes and ~ 2 times the temporal length (in this case ~ 4 hours) and with vertical wavelengths $\lambda_z = 2\pi/|m|$ between 2 km and ~ 30 km. This defines our observational window [e.g., Alexander, 1998] on the full two-dimensional gravity wave power spectrum of relative density perturbations, $F_\rho(m, \Omega)$, as afforded by these lidar measurements and the analysis technique. It should be noted that this processing technique is slightly different than that presented in GKT98 (e.g., different filter cut-offs, different error estimation), but the qualitative variations are unchanged and even the quantitative values are similar. In both processing methods, the gravity waves extracted from the lidar data were consistently quasi-monochromatic with vertical wavelengths $\lambda_z \sim 10$ km and observed periods $T \sim 2.5$ hours [GKT98]. These observed characteristics help constrain the gravity wave source spectrum, as discussed next.

3. GROGRAT Model and the Tropospheric Source Spectrum

[13] The Gravity Wave Regional or Global Ray Tracer (GROGRAT) is a ray-tracing model that tracks the propagation and amplitude evolution of gravity waves through the lower and middle atmosphere. The core ray formulation and initial model are described by Marks and Eckermann [1995]. Eckermann and Marks [1997] describe an updated version of the model. GROGRAT traces waves using ray equations based on a fully nonhydrostatic rotating dispersion relation. Wave amplitudes are tracked along ray paths using wave action conservation methods, subject to dissipation due to scale-dependent infrared radiative damping [Zhu, 1993], turbulent diffusion [Pitteway and Hines, 1963] and saturation due to convective/dynamical instabilities [Fritts and Rastogi, 1985]. In these experiments, nondissipating gravity waves conserved their vertical flux of wave action density (proportional to Eliassen-Palm flux). Com-

puted ray paths were fully three-dimensional and included wave number refraction due to both horizontal and vertical gradients in the background atmosphere, but time variations were not included in the ray calculations. WKB violations are flagged due to waves that reflect vertically near turning points or encounter critical levels.

[14] GROGRAT requires a gridded background atmosphere through which it traces waves. For this study we used the NCEP-CIRA data on a $2.5^\circ \times 2.5^\circ$ grid (see section 2) within the region 280° – 340°E , 52.5° – 82.5°N , centered near Sondrestrom. We used GROGRAT to fit and regrid the gridded pressure-level atmospheric data onto 40 equispaced geometric altitude levels separated vertically by 2.5 km.

[15] To specify a plausible tropospheric source spectrum of gravity waves for GROGRAT experiments during August 1996 and summer 2001, we first constrained potential candidate waves based on the observational window of the Sondrestrom lidar observations. We began by specifying a full spectrum of gravity waves directly over Sondrestrom at a nominal lidar observation altitude of 40 km [GKT98; Gerrard et al., 2004]. This spectrum comprised the set of all possible waves with ground based periods T of 2, 2.5, and 3 hours (all within the lidar observational window) and 13 possible horizontal wavelength components in the x or y directions, λ_x and λ_y , of ∞ , 800, 700, 600, 500, 400, 300, 200, 100, 50, 25, 12.5, and 6.25 km. Each of these horizontal wavelength values can be positive or negative, which serves to specify, equivalently, a set of total horizontal wavelengths λ_h and horizontal propagation azimuths. This resulted in a spectrum of $13 \times 13 \times 4 \times 3 - 1 = 2027$ rays (the -1 comes from eliminating the unphysical $\lambda_x = \infty$, $\lambda_y = \infty$ ray). This broad distribution of horizontal wavelengths was chosen so that a full range of vertical wavelengths was generated, which yielded some waves that had the potential to be observed within the lidar's observational vertical wavelength window of 2–30 km. Note that none of these gravity waves are stationary ($T = \infty$), consistent with the notion that quasi-stationary mountain waves cannot enter the summer extratropical upper stratosphere [Bacmeister, 1993].

[16] The RMS horizontal wind amplitudes of the waves were initially all set to 4 m s^{-1} and then scaled with vertical wave number m to yield a +3 power spectral index over the range $m = 0$ to a typical upper stratospheric characteristic wavelength [Smith et al., 1987] $2\pi/m^* \sim 8$ –12 km (as opposed to the often observed +2 spectral index in this range). At high vertical wave numbers we imposed a -7 spectral index as opposed to the usual m^{-3} power law from the characteristic wavelength to higher wave numbers of the horizontal velocity power spectrum as a function of vertical wave number [e.g., Dewan and Good, 1986; Smith et al., 1987; Weinstock, 1990; Fritts and Alexander, 2003]. This input vertical wave number spectrum is depicted with asterisks in Figure 2. The selection of these steeper power laws is based on the quasi-monochromatic waves observed by lidar in the summer upper stratosphere over Sondrestrom, which typically have vertical wavelengths between 8 km and 12 km, and little variance at shorter or longer wavelengths. Note that other source spectra, with spectral indices that varied considerably across the possible ranges, including the traditional shallow spectrum in Figure 2

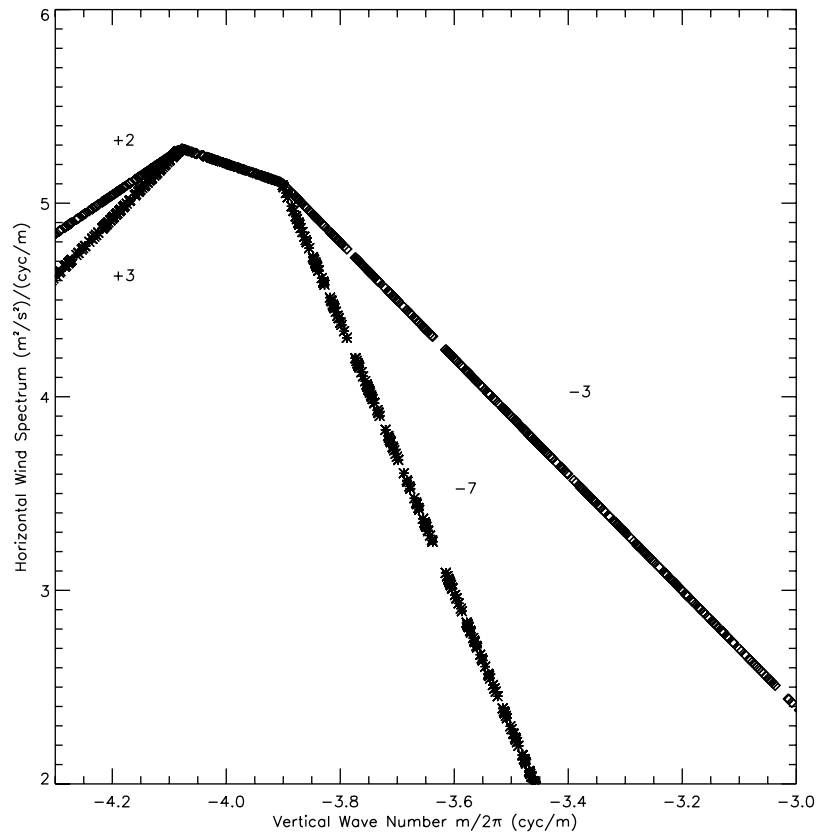


Figure 2. Power spectral density as a function of vertical wave number m (asterisks) for gravity waves backtraced from a starting altitude of 40 km over Sondrestrom, Greenland on August 5th, 1996. The natural logarithm was taken of both the power density and the vertical wave number (in cyc m^{-1}) and the axis scales reflect these quantities. This curve takes the power law form m^{+3} at small m and m^{-7} at large m . A power spectral density curve with power law forms of m^{+2} and m^{-3} at small and large m , respectively, are shown for comparison (diamonds). Though the results obtained with the steeper spectrum are discussed in this paper, results obtained with other spectral shapes are very similar.

(diamonds), yielded similar results to those which will be reported in Section 4 and only slightly altered the results in Section 5. In this paper, we present only the results using the steeper source spectrum.

[17] This spectrum of gravity waves at 40 km was then propagated backwards in time (i.e., downwards in altitude) in an effort to locate both potential wave sources and locations in the troposphere; so-called “reverse ray tracing” or “backtracing”. The waves were propagated back down to ~ 6 km, an arbitrary generation height chosen for this study: variation of this altitude by ± 2 km did not make a noticeable impact on subsequent model results. Figure 3 shows an example of this backtracing procedure for August 5th, 1996 for the 12 UT sounding. A total of 471 rays ($\sim 23\%$ of the initial 2027 rays) were able to propagate down to the troposphere while remaining within the regional model domain. We see that there is a broad geographical distribution of tropospheric locations from which waves that propagate to 40 km over Sondrestrom could have originated. Approximately 18% of the initial rays were traced to a region outside of the model domain: these are located mainly in the east-west wedge of missing ray paths in Figure 3 and shows that most of these missing waves propagate outside the imposed longitude range rather than

the latitude range. All other rays were dissipated (53%) or violated WKB ray-tracing conditions (6%) sometime during the ray-tracing process and thus, assuming troposphere-only sources, cannot account for observed waves in the lidar data at 40 km.

[18] Rays that made it down to 6 km and were still within the regional domain were then assumed to comprise the tropospheric source spectrum. This source spectrum was then put back into the model at 6 km on August 5th, 1996, and propagated back up through the same atmospheric background conditions (forward ray-tracing) to their common point over Sondrestrom at 40 km, then onward until they reached 80 km or were removed by excessive dissipation, critical levels or turning points. Surviving ray paths at 80 km are plotted in Figure 4. Solid diamonds in Figure 4 show source level locations, and reveal that only those waves generated to the west of Greenland reach the mesosphere over Sondrestrom.

4. Ray Modeling Results for August 1996

[19] The tropospheric source spectrum at 6 km, determined solely from the atmospheric background conditions of August 5th, 1996 using backtracing procedures, was

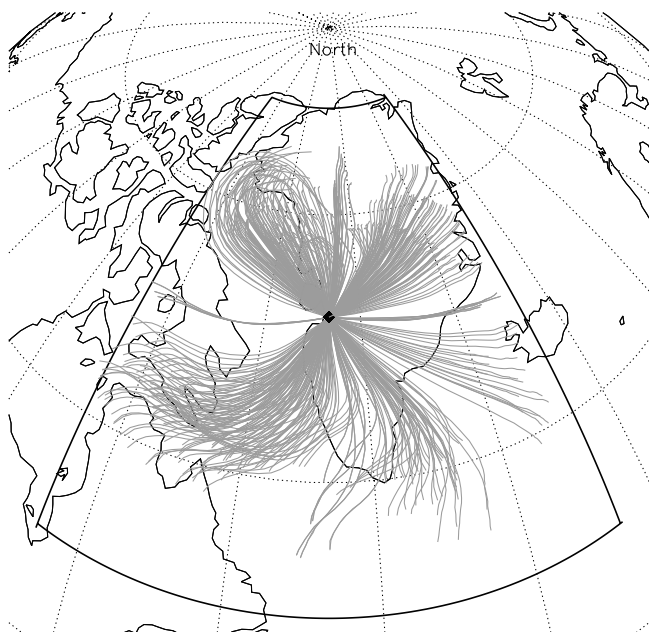


Figure 3. Backtraced (reverse ray traced) group trajectories of the gravity wave spectrum in Figure 2 on August 5th, 1996 (12 UT). Only gravity waves that stayed within the model domain (in dark black lines) and made it to 6 km are plotted. Dark diamonds represent initial location of each gravity wave (all located above Sondrestrom at 40 km altitude in this case). Latitude-longitude gridlines are spaced every 15° . See color version of this figure at back of this issue.

traced upwards for all subsequent days of August 1996 for which there were lidar data available for comparison. By fixing the source spectrum and other model parameters while allowing only background atmospheric conditions to vary each day, these model experiments test the potential for the regionalized gravity waves observed on August 5th to propagate to 40 km and eventually 80 km on the other August days. Thus we have not included generation of waves from other transient sources that may come and go as weather patterns change, and have also excluded waves originating from outside the model domain, such as potentially ducted waves in the mesosphere.

[20] For days after August 5th, we needed to establish criteria for determining if a particular gravity wave ray that reached 40 km would be observable by the molecular/aerosol lidar. The criteria that were imposed were:

[21] 1. Rays must be within 555 km horizontal distance of the lidar site ($\sim 5^\circ$ latitude, 13° longitude).

[22] 2. Rays cannot have a vertical wavelength $\lambda_z > 20$ km at an altitude of 6 km, as gravity waves with longer vertical wavelengths are not usually seen in the troposphere (though we note that this may be an observational sampling problem, due to the experimental difficulty resolving these types of tropospheric waves). Increasing the allowed vertical wavelength did not impact the results reported here.

[23] 3. Rays must take no longer than 16 hours to propagate to 40 km, as model runs were separated by 12 hours, plus a two-hour window on either side.

[24] 4. Rays must have a ground-based horizontal phase speed $c_h = \lambda_h/T < 70 \text{ m s}^{-1}$, as faster gravity waves are less likely to be generated in the extratropics.

[25] 5. Rays at 40 km must have $2 \text{ km} < \lambda_z < 30 \text{ km}$ and $30 \text{ min} < T < 4 \text{ hours}$ in order to be resolved in the lidar data.

[26] 6. Rays must be able to propagate to 55 km. We also needed to establish separate criteria for wave activity at 80 km. They were:

[27] 7. Rays at 80 km must be within 1111 km horizontal distance of the lidar site (approximately 10° latitude, 25° longitude).

[28] 8. Rays cannot have $\lambda_z > 20$ km at an altitude of 6 km.

[29] 9. Rays must take no longer than 16 hours to propagate to 80 km. This allows us to focus on the fast [short period] waves indicated by the results of *Gerrard et al.* [2004].

[30] 10. Rays must have a ground-based horizontal phase speed $c_h < 70 \text{ m s}^{-1}$.

[31] 11. Rays must have an intrinsic period $T_{\text{int}} = 2\pi/\omega < 6$ hours. Modeling suggests this condition is necessary for MC destruction by gravity waves [*Rapp et al.*, 2002].

[32] We note that these are separate, exclusive criteria: a modeled wave did not have to satisfy both conditions in order to be retained at a particular altitude. There are certainly waves that were “observed” by the lidar at 40 km that were not observable at 80 km; for example they

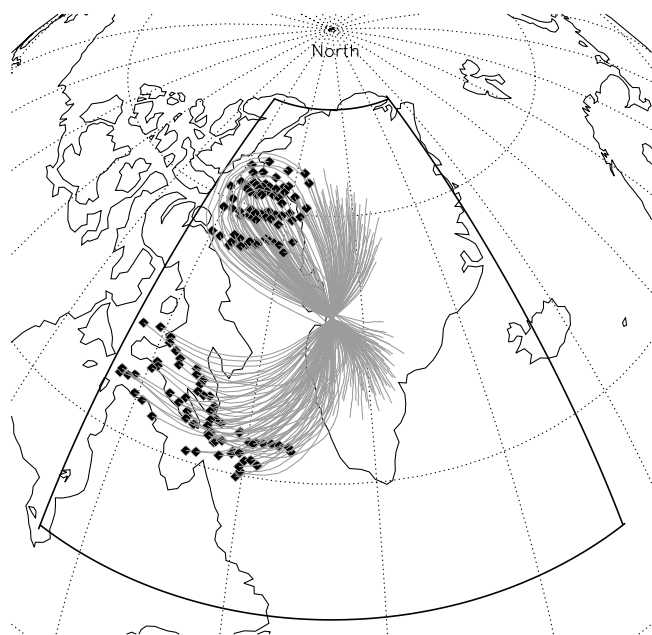


Figure 4. Gravity wave ray group trajectories initiated with the tropospheric spectrum obtained at 6 km from Figure 3 on August 5th, 1996. As expected, all rays converge to a single point over Sondrestrom at 40 km. The waves were then allowed to propagate further in altitude/time, and only gravity waves that reached 80 km and satisfied observability criteria are plotted. Dark diamonds represent the initial location of each gravity wave in the troposphere. Latitude-longitude gridlines are spaced every 15° . See color version of this figure at back of this issue.

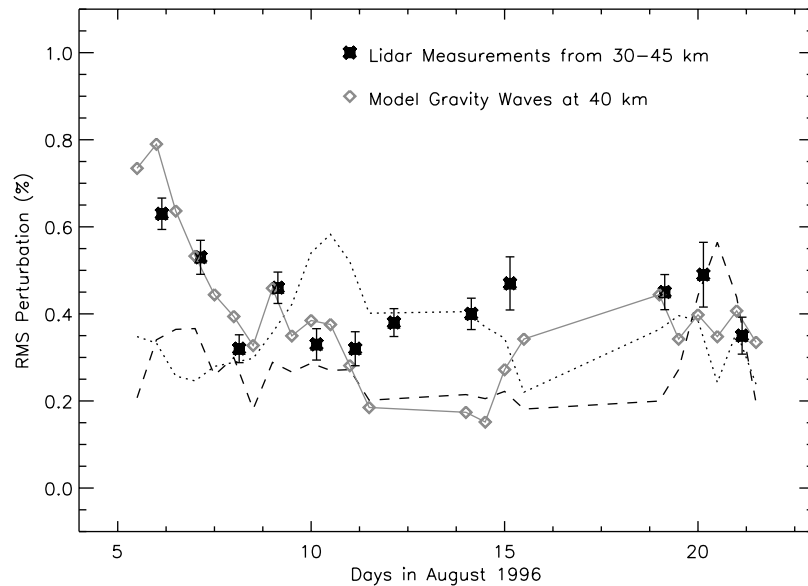


Figure 5. Upper stratospheric gravity wave activity as quantified by RMS relative density perturbations in the lidar observational window (see text) over Sondrestrom, Greenland for each day in August 1996. The black data points with one standard deviation bars represent the lidar observations. These observed values are compared to modeled gravity wave activity as represented by the gray line. The dotted line and dashed line represent model results based on a gravity wave source spectrum generated from backtraced runs on August 10th and August 20th, 1996, respectively.

were dissipated or propagated obliquely away from the lidar site. Likewise, there were waves that were observable at 80 km that were not observable at 40 km. Thus, when we later compare and correlate the gravity wave fields between the two altitudes, a direct comparison of the wave amplitudes is inappropriate because the number of waves in the observable wave field is different

[33] For those gravity waves that satisfied these “observability” criteria at the 40-km and/or 80-km levels, their peak horizontal velocity amplitudes were added, then normalized by the total horizontal velocity amplitude that would have arisen had all of the initial 471 gravity waves made it to 40 km or 80 km (i.e., the maximum possible total induced wind perturbation at 40 km, assuming no wave saturation is $471 \text{ rays} \times 4 \text{ ms}^{-1} = 1884 \text{ ms}^{-1}$). This yields a final fractional amplitude value that was multiplied by a scaling constant at 40 km or 80 km to give a very coarse estimate of the induced horizontal wind perturbations from this wave spectrum. We scale this value linearly to account for the conversion (via the gravity wave polarization equations) from horizontal wind amplitudes to relative density perturbations measured by the lidar and from peak amplitudes to RMS quantities. Finally, we applied an invariant multiplicative constant to scale the final model values to yield absolute values similar in range to the lidar-obtained RMS relative density perturbations, to better facilitate a direct comparison of lidar-observed and model-generated wave activity measures.

[34] Figure 5 plots lidar and model wave activity time series at 40 km, the latter derived after tracing the source spectrum upwards for the remaining days of August 1996. We see quite good agreement between model and data from the 6th to the 11th and on the 18th to the 21st. We note that the modeled gravity wave activity decreases with time

during August, then increases again toward the end of the month. This latter increase is consistent with gravity wave variance increases through August observed over Sondrestrom [Gerrard *et al.*, 2000]. The linear correlation coefficient (r) between the model results and the lidar data is ~ 0.75 using either a Fisher- z test or a Student’s t -test, both of which are well within the 95% confidence interval. Hence, we conclude that this model experiment shows some skill in reproducing observed upper stratospheric gravity wave activity observed by the lidar in August 1996.

[35] The rays for the 6th and 11th that satisfied criteria for observability at 80-km altitude are plotted in Figures 6 and 7 respectively. On inspection of wave activity during the 6th, we see that the rays that reached 80 km originated from the northern Labrador Bay-Hudson Strait region ($\sim 300^\circ\text{E}$, $\sim 61^\circ\text{N}$) and northwest Greenland-Baffin Bay area ($\sim 295^\circ\text{E}$, $\sim 73^\circ\text{N}$). These ray groups propagated obliquely eastward up into the stratosphere where they were subsequently refracted to propagate more vertically to affect the MCs above. This upward refraction can be deduced from strengthening easterly winds in the upper stratosphere and mesosphere (e.g., Figure 1), which cause eastward-propagating gravity waves to refract to longer vertical wavelengths and attain faster vertical group velocities, causing them to propagate rapidly into the mesosphere. Conversely, westward-propagating gravity waves generated to the east of Sondrestrom were strongly refracted toward critical levels in the strengthening upper stratospheric easterlies and so these waves had little impact at 40 km over Sondrestrom and still have a regional impact on the mesosphere over this site. On August 11th, we

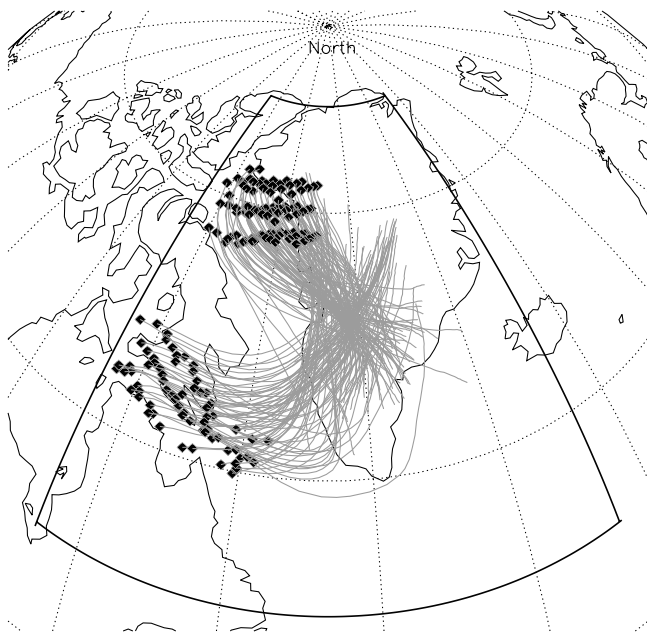


Figure 6. Gravity wave ray group trajectories initiated at 6 km with the tropospheric spectrum obtained from Figure 3 on August 6th, 1996. Only gravity waves that met the 80 km observability criteria are plotted. Dark diamonds represent the initial location of each gravity wave in the troposphere. Latitude-longitude gridlines are spaced every 15° . See color version of this figure at back of this issue.

found that very few waves were able to make it either to 80 km or 40 km, suggesting that there was less potential influence of gravity waves at all altitudes above Sondrestrom.

[36] One notes from Figure 5 that from August 12th–15th, the model experiments predict gravity wave values that are much lower than those observed. This may be due to a lack of representation of new different gravity wave sources that have developed in the troposphere at these later times. Inspection of geopotential height maps for these days (not shown here) reveals a transient surface low developing to the southeast of Greenland, which may have provided a new tropospheric wave source that temporarily generated more gravity wave activity at 40 km. Additionally, the assumptions made about the original source spectrum and the various 40 km acceptance criteria may also contribute to these model/data discrepancies.

[37] Variable rejection criteria at 40 km and 80 km mean that the subsets of observable model-generated waves at each altitude are not the same, and thus the two wave fields might be poorly correlated. To test this, Figure 8 show scatterplots of our modeled gravity wave values at 40 km and 80 km during August. We see a strong correlation between the values at the two altitudes, with a linear correlation coefficient of 0.96. Such high correlation is consistent with gravity waves at 40 km rapidly propagating to 80 km due to enhanced upward refraction by intensifying easterlies and remaining above the lidar site at both altitudes.

[38] Based on model output, the gravity waves satisfying both the 40 km and 80 km observability criteria before

August 10th tended to have horizontal wavelengths $\lambda_h \sim 350$ km and vertical wavelengths $\lambda_z \sim 13$ km at an altitude of 40 km, and $\lambda_z \sim 8$ –15 km at an altitude of 80 km. We found that it typically took ~ 4 –5 hours for such gravity wave rays to propagate from 40 km to 80 km as determined by the vertical group velocity. After August 10th, the gravity waves had $\lambda_h \sim 200$ km and $\lambda_z \sim 9$ km at an altitude of 40 km, $\lambda_z \sim 15$ km at an altitude of 80 km, and took ~ 6 hours to propagate from 40 km to 80 km. The difference in wave characteristics between early August and mid- to late August is due to the removal of longer horizontal and vertical wavelength waves from the spectrum below 40 km due to changes in background atmospheric wind patterns.

[39] About 57% of the modeled gravity waves at 80 km are still stable (i.e., they are not “breaking” or “saturated”). Furthermore, the onset of instability for most of the saturated waves occurred only within the top 10 km of the model domain. Therefore, as a whole, the gravity wave field is still experiencing amplitude growth in order to conserve vertical action flux densities. This is interesting given the relatively large gravity wave horizontal velocity amplitudes of ~ 4 m s $^{-1}$ imposed at 40 km (for a background wind of ~ 15 m s $^{-1}$). This stability is consistent with enhanced vertical refraction from 40 km to 80 km, since long vertical wavelengths make wave saturation amplitudes much larger and thus tend to keep long wavelength wave fields stable to higher altitudes in the atmosphere [Smith et al., 1987]. These stability characteristics are determined by local CIRA-86 climatological mesospheric winds, whereas actual mesospheric winds

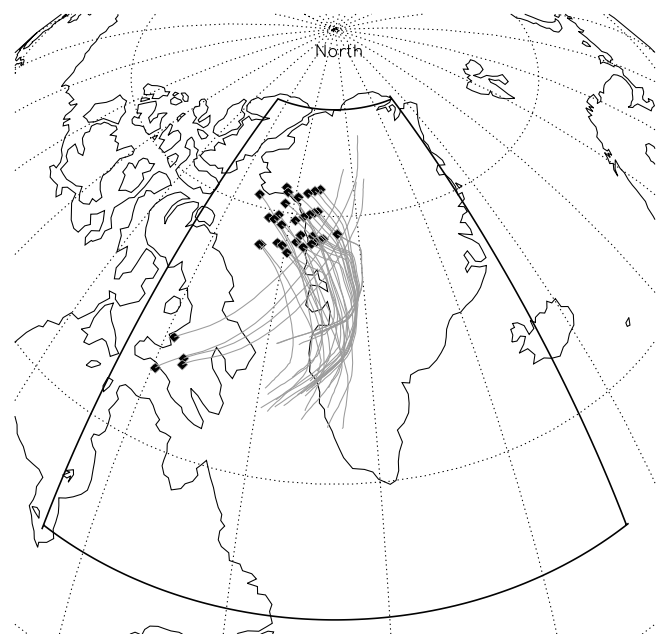


Figure 7. Gravity wave ray group trajectories initiated at 6 km with the tropospheric spectrum obtained from Figure 3 on August 11th, 1996. Only gravity waves that met the 80 km observability criteria are plotted. Dark diamonds represent the initial location of each gravity wave in the troposphere. Latitude-longitude gridlines are spaced every 15° . See color version of this figure at back of this issue.

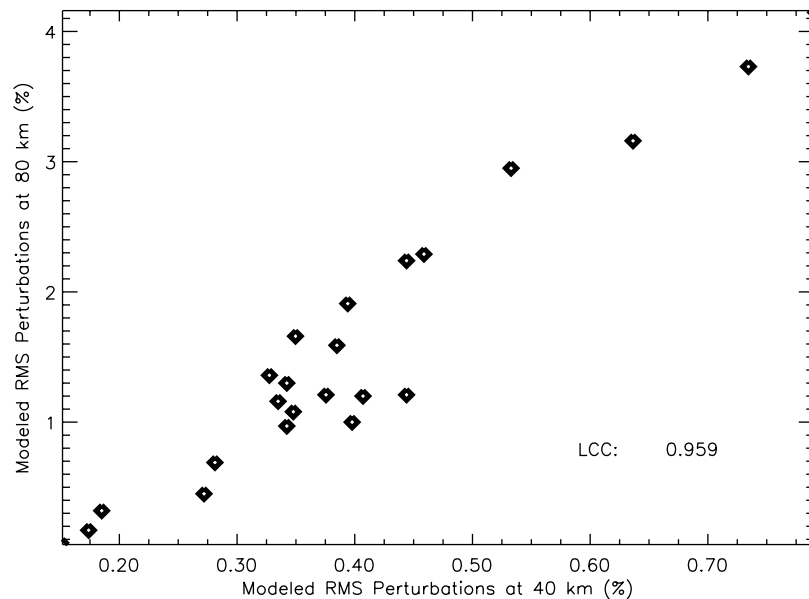


Figure 8. Scatterplot of gravity wave activity at 40 km versus gravity wave activity at 80 km as computed from the ray tracing model experiments during August 1996. The linear correlation coefficient (LCC) is 0.96. See text for further details.

(and hence wave amplitude characteristics) are likely to have been more variable in reality.

4.1. Discussion of Model Experiment Results

[40] The model results are robust to variations in several different model run parameters. Changes in atmospheric grid size and spacing, source characteristics (e.g., different spectral slopes, different tropospheric start altitudes, different initial horizontal wind velocities), and upper level observability/rejection criteria (e.g., time for rays to get to their respective levels, proximity to Sondrestrom) changed actual numerical values for model runs during August period, but the qualitative aspects of the results remained unchanged in all cases.

[41] In addition, we computed tropospheric source spectra for days other than August 5th using our back-tracing procedure described in section 2. It is important to note that using any such source spectra generated on any day in August, other than 5th through the 6th, yielded model results that were inconsistent with observations and do not reproduce the observed daily structure. For example, Figure 5 also plots results from model runs using source spectra generated on August 10th and August 20th, using the same scaling factors as before. We note that both of these source spectra yield results that do not come close to matching the experimental results. Source spectra generated on August 6th closely resembled earlier model results that used an August 5th source spectrum. We also note that model runs for these three source spectra each yield model wave activity time series that peak on the specific day that each source spectrum was generated and then decrease to lower values before and after. This shows that these source spectra are tuned to give source-level waves with maximum stratospheric transmissivity characteristics for these particular days.

[42] We theorize that the reason for the good comparison of model results and observations for source spectra obtained on the 5th through the 6th is because of the unusual geophysical conditions present on those days. After investigating a >4-year climatology of summer gravity wave observations with the Sondrestrom lidar [Gerrard *et al.*, 2000], we noted that gravity wave activity around August 5th–6th 1996 was unusually strong. Thus, we assume that the gravity wave activity on these days represents a maximum potential for gravity wave transmission into the stratosphere over Sondrestrom in August, and that it is comprised of gravity waves from some of the dominant sources in this region for this time of year. Source spectra models generated on other days from more typical levels of wave activity at 40 km would thus always be lacking crucial gravity wave components which can reach the stratosphere at more active times, and would therefore not be able to reproduce essential features displayed in the observations throughout the summer as transmission characteristics change.

[43] With the assumption that this source spectrum represents an acceptable first-order working approximation for some of the gravity waves sources in this specific region at this specific time of the year, we note from inspection of Figures 3 and 6 (and more importantly the consistency between observations and model results) that there seem to be certain geographic regions where gravity waves could have plausibly been “quasi-continuously” generated throughout this August period. Geopotential height maps from August 6th in Figure 9, for example, show a low pressure cell over northwest Greenland and the Baffin Bay region (~ 1000 km northwest of Sondrestrom). In addition, there appear to be indications of potential frontal activity over the Labrador Sea region (~ 1000 km southwest of Sondrestrom). Since these types of weather systems can generate gravity waves [Fritts and Alexander, 2003], one

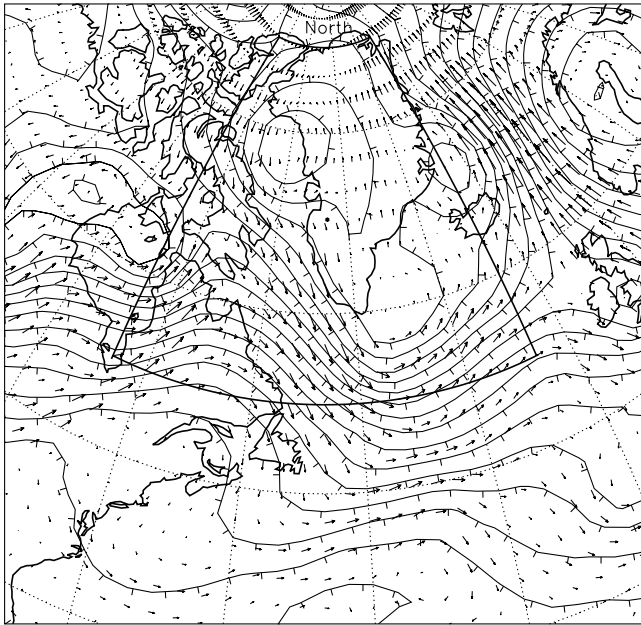


Figure 9. Synoptic map at the 700 hPa level (~2.5 km) from NCEP analysis on August 6th, 1996. Thin black lines are contours of constant geopotential (with perpendicular ticks pointing toward higher geopotential), while vectors represent assimilated winds. Latitude-longitude gridlines are spaced every 15°.

might suspect regional production of waves from these specific tropospheric regions. Later, in the geopotential height maps for August 11th (Figure 10), no such corresponding structure is present to the west of Sondres-

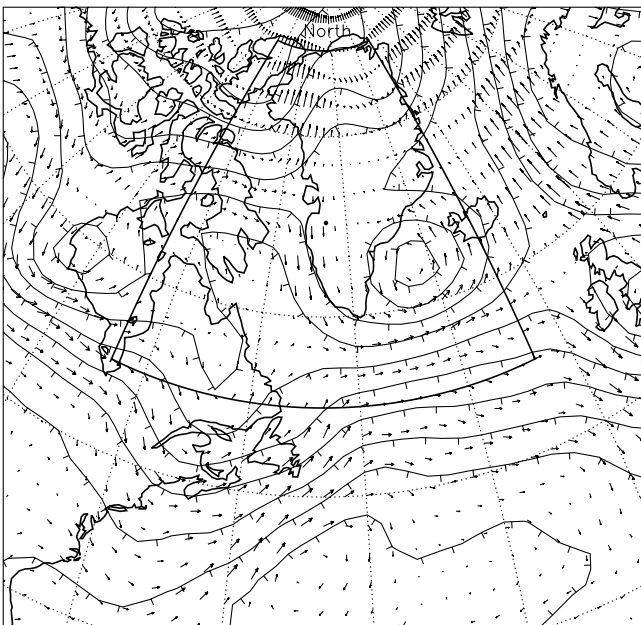


Figure 10. Synoptic map at the 700 hPa level (~2.5 km) from NCEP analysis on August 11th, 1996. Thin black lines are contours of constant geopotential (with perpendicular ticks pointing toward higher geopotential), while vectors represent assimilated winds. Latitude-longitude gridlines are spaced every 15°.

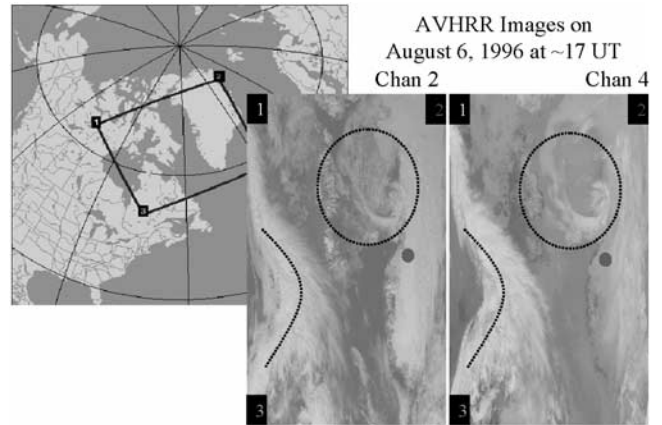


Figure 11. Data from AVHRR channels 2 (visible-near infrared) and 4 (far infrared) on August 6th, 1996 at ~17 UT. For ease of orientation, the numbering on the map corresponds to the numbering on the images. The Greenland ice shelf and the coast are visible on the right in these images. See color version of this figure at back of this issue.

strom (waves generated to the east of Sondrestrom, particularly near the cutoff low to the southeast, are the exception). Imagery from channel 2 (visible-near infrared) and channel 4 (far infrared) of the Advanced Very High Resolution Radiometer (AVHRR) on August 6th and 11th (each taken at ~17 UT) are presented in Figures 11 and 12, respectively. Inspection of tropospheric cloud structure in the images from the 6th confirmed that there was a low pressure cell with associated frontal activity in the northwest Greenland-Baffin Bay region, as well as frontal activity in the northern Labrador Sea-Hudson Strait region, at this time. Though these atmospheric phenomena are individually transient in nature, they develop recurrently, making these geographical regions climatologically active in regards to convective systems and frontal storm tracks [e.g., Hurrell *et al.*, 2003; and references therein]. Similar inspection of AVHRR

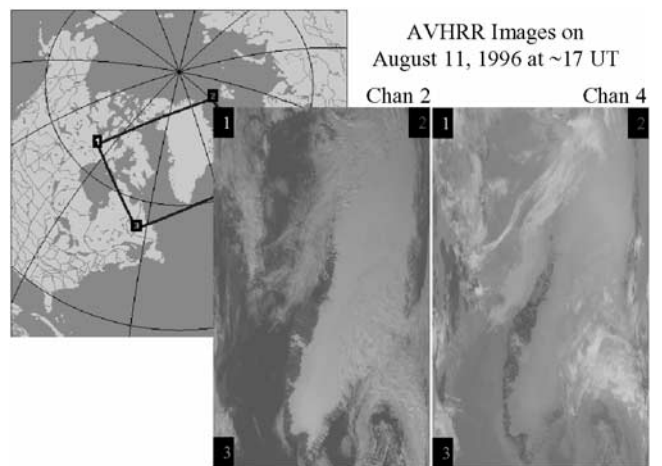


Figure 12. Data from AVHRR channels 2 (visible-near infrared) and 4 (far infrared) on August 11th, 1996 at ~17 UT. For ease of orientation, the numbering on the map corresponds to the numbering on the images. The Greenland ice shelf and the coast are visible on the right in these images. See color version of this figure at back of this issue.

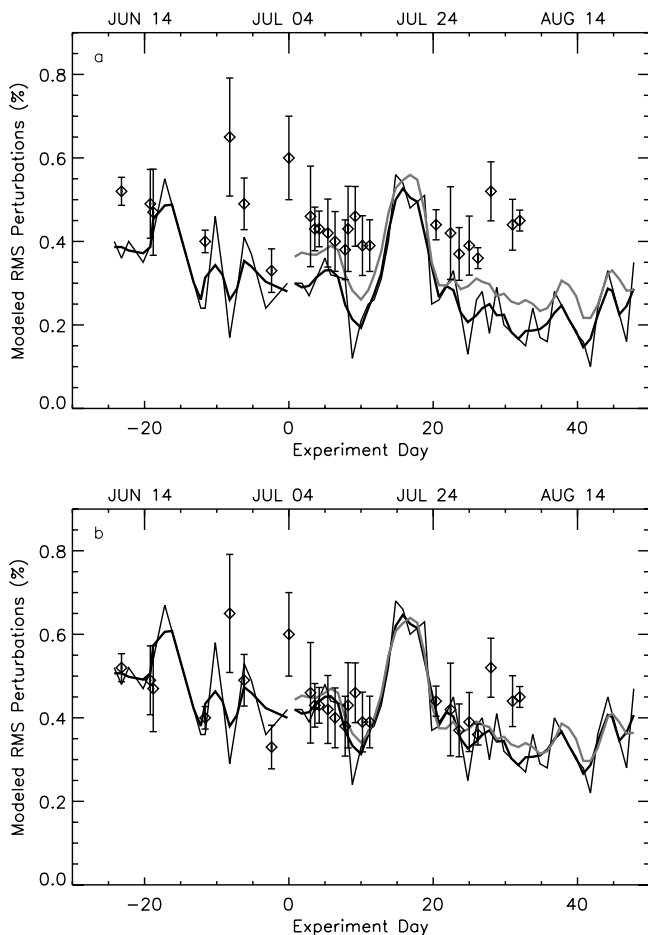


Figure 13. (a) Diamonds represent upper stratospheric gravity wave activity for summer 2001 as RMS relative density perturbations within an observational window (see text) near 40 km over Sondrestrom, Greenland as measured by the molecular/aerosol lidar (points with one standard deviation bars). The raw activity from GROGRAT model experiments is plotted with a thin black line. A three day running mean of these data is plotted with a thick black line. The thick gray line is a three-day running mean of the average of model output using NCEP analyses, 1-day forecasts, and 2-day forecasts as a background. The x axis is experiment day, with day 1 corresponding to July 5th, 2001. Analyses before experiment day 1 did not include forecast information. (b) As for panel (a), but with the raw GROGRAT model data and a three day running mean of these data offset vertically by +0.12. The thick gray line is a three-day running mean of the average of the model output using analyses, 1-day forecasts, and 2-day forecasts, offset vertically by +0.08.

data from the 11th indicates that these specific atmospheric conditions were less active, and thus the potential for gravity wave generation by convective and/or frontal activity had deteriorated.

4.2. Discussions of Model Experiment Results on MCs

[44] On the question of the interaction of gravity waves with MCs, the model-based values of upper stratospheric

to mesospheric propagation times are consistent (to within a factor of 2) with earlier estimates by GKT98 based on observations alone, as well as with *Gerrard et al.* [2004] using July 2001 observations. However, since the modeled propagation time is somewhat larger than the $\sim 1\text{--}4$ hour propagation time inferred from observations, the model results do not help us conclusively resolve the physical mechanisms controlling the phase-lagged relationship between upper stratospheric gravity wave activity and overlying MCs discussed by *Gerrard et al.* [2004]. While the model experiments support the concept of a direct quasi-vertical influence of gravity waves at 40 km on the overlying MC field via increased vertical group velocities, we cannot exclude the possibility that the two fields are related in some other way or that the correlations noted in earlier studies are fortuitous and thus spurious. Since the model gravity waves were largely unsaturated at 80 km, then the wave breaking effect on MCs discussed by *Fritts et al.* [1993] and *Gerrard et al.* [2004] is largely absent for these waves. This leaves only the influence of the temporal wave-induced temperature oscillations, which implies reductions in particle size and overall brightness [*Rapp et al.*, 2002] and thus a negative influence on overlying MCs, as observed [e.g., *Thayer et al.*, 2003; *Gerrard et al.*, 2004].

5. Model Experiments and Discussion for Summer 2001

[45] To study these issues further, we conducted near-real-time model experiments using NCEP forecast data as a background during summer 2001. The same tropospheric gravity wave source spectrum discussed in Section 3 and used in Section 4 was used in these experiments. Rays were propagated upwards by the model on 77% of the days from July 5th, 2001 (referred to as experiment day number 1) to August 21st, 2001 (experiment day number 48). Forecasts were not run on the missing days because of networking issues which prevented numerical forecast data from being downloaded for real-time runs. The 40 km and 80 km detection criteria (outlined in Section 4), as well as the constant used to scale the model gravity wave activity to the lidar-derived values, were also unchanged. A linear interpolator in time was used to fill in model results for any missing days. The modeled gravity wave activity was posted daily on the world-wide web as a test forecast/analysis product for the lidar and general community inspection. Lidar data throughout the summer were acquired and analyzed after the forecasting period in September, and were therefore not reported in near-real-time.

[46] The ray-tracing model results based on the AVN analyses are plotted in Figure 13a, along with the lidar-derived data (diamonds with error bars). The raw model data are plotted with a thin black line, and a three day running mean of these data is plotted with a thick black line. The thick gray line is a three-day running mean of the average of the model output using NCEP AVN analysis, 1-day forecast, and 2-day forecast fields lower down. Note that although lidar data were acquired at Sondrestrom throughout June of 2001, the ray-tracing model was not running at that time and AVN forecasts

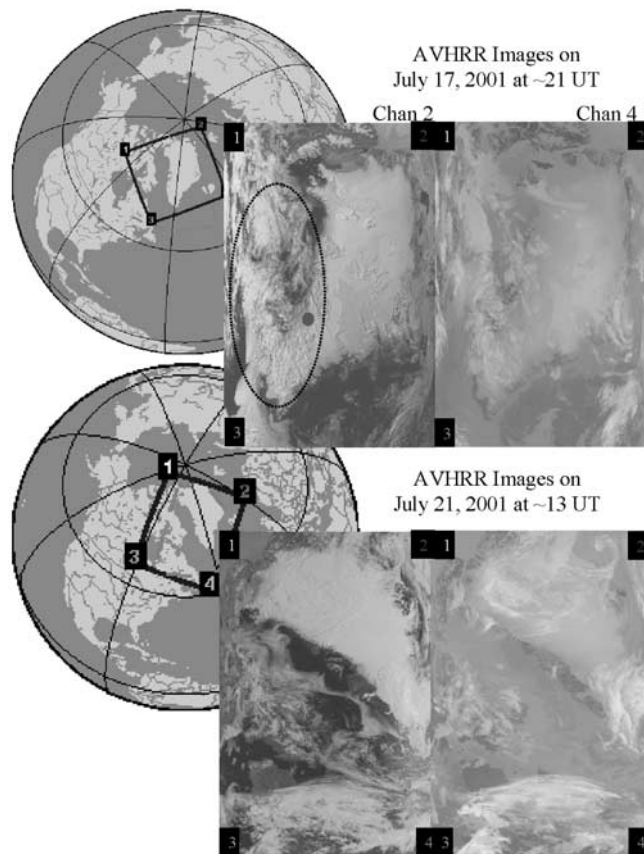


Figure 14. Data from AVHRR channels 2 (visible-near infrared) and 4 (far infrared) on experiment day 13 and day 17 (July 17th and July 21st of 2001, respectively) at ~ 21 UT. For ease of orientation, the numbering on the map corresponds to the numbering on the images. The Greenland ice shelf and the coast are visible on the top-right in these images. The dashed red line represents the model boundary. These data are representative of similar data observed during this period. See color version of this figure at back of this issue.

were not obtained. Thus, model curves based on forecast data are absent from Figure 13 in June. NCEP analyses from the NCAR-SCD were obtained after the forecasting period for comparison to the June lidar observations, and are also presented in Figure 13 for completeness.

[47] Comparing modeled and measured upper stratospheric gravity wave activity in Figure 13a, we see a constant offset between the various model time series and the observations. We remove this offset somewhat arbitrarily by adding 0.12 to the modeled gravity wave activity from analyses (black curves) and 0.08 to averaged model wave activity from runs using analyses and forecasts (gray curve): results are shown in Figure 13b. These offsets are qualitatively consistent with 1996 results in Figure 5, which showed that sources tuned (via backtracing experiments) for various days in August yielded large model activity on those days, then reduced by ~ 10 – 50% on other days. The 5th August 1996 source used here produces reduced activity for 2001 since it is not tuned for any specific 2001 events.

[48] The correspondences between model and data in Figure 13b are mixed: the linear correlation between the two curves is ~ 0.50 . If four or five of the large-amplitude data events are removed, the linear correlation coefficient greatly increases, though there is no justifiable reason for excluding these data points. From June through early July, the modeled gravity wave activity agrees quite well with the lidar measured gravity wave activity (within the range of the uncertainty bars). During days 20–28 (July 24th to August 1st), the model and data also match well. Around day 29 (August 2nd), however, the lidar data show an increase in gravity wave activity, consistent with previous measurements which suggest an increase in gravity wave activity at 40 km during August over Sondrestrom [Gerrard *et al.*, 2000]. The model runs do not simulate this feature. This suggests lack of proper representation of particular gravity wave sources which produce these punctuated enhancements in observed activity. In addition, RMS lidar values obtained after day 29 (August 1st) are abnormally large: further inspection of the lidar data on these dates indicates poor system performance (e.g., non-linear receiver caused by high solar background) that may have artificially enhanced the measured variability.

[49] Model-generated gravity waves that satisfied observability criteria at both 40 km and 80 km typically had horizontal wavelengths $\lambda_h \sim 200$ km and vertical wavelengths $\lambda_z \sim 10$ km at an altitude of 40 km. Such waves typically took ~ 6 hours to propagate from 40 km to 80 km. As opposed to the model results from August 1996, a smaller fraction of these gravity waves were unsaturated ($\sim 45\%$), and so many waves were saturated at 80 km, having begun saturating at around 60 km. This model result supports the suggestion [Gerrard *et al.*, 2004], that gravity waves can impact MCs on timescales of less than a day by at least two physical mechanisms: their temperature perturbations [e.g., Rapp *et al.*, 2002] and localized wave breaking that drives synoptic-scale upwelling and an adiabatic cooling response.

[50] One of the difficulties in comparing the lidar data to the model results in Figure 13b is missing data during key periods, such as days 12–19 (July 16th–23rd) when the model experiments predicted enhanced activity. To address the environmental factors behind both the missing lidar data and the increases in modeled gravity wave activity, we analyze AVHRR imagery over the region during this period. Figure 14 plots AVHRR images from channel 2 (visible-near infrared) and channel 4 (far infrared) on experiment days 13 and 17 (July 17th and July 21st, respectively) at ~ 21 UT and 13 UT, respectively. They show evidence of convective or frontal tropospheric activity in the Labrador Sea and Baffin Bay region. In addition, we see high tropospheric cloud cover during this period near Sondrestrom. The images, to some degree, show why there are no lidar data during this period of July, as the cloud cover attenuated the lidar signal. One might also expect higher than usual tropospheric gravity wave generation associated with this convective activity. Indeed, during the observational forecasting campaign, we knew from these model forecast runs that high gravity wave activity was being modeled during this period, and so we tried to prepare for more

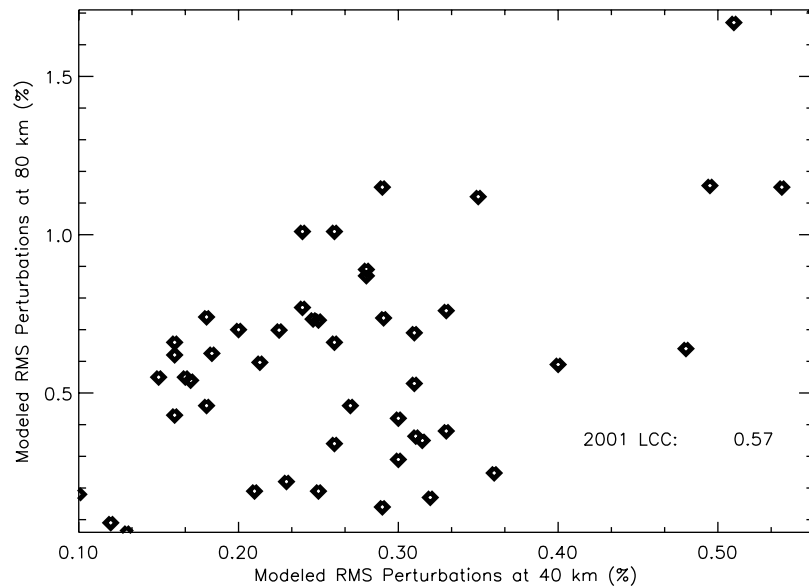


Figure 15. Scatterplot of gravity wave activity at 40 km with gravity wave activity at 80 km from summer 2001 as computed from ray-tracing model experiments (the data are neither smoothed nor scaled). The linear correlation coefficient (LCC) is 0.57. See text for further details.

extensive, continual lidar observations during this period (without success). Note that the model enhancements on days 12–19 are not due to source effects, since the source remains constant: rather, it is due to increased transmission of the set tropospheric wave spectrum to 40 km.

[51] The modeled gravity wave activity at 40 km is compared to the modeled gravity wave activity at 80 km in Figure 15 using model output from AVN analyses after experiment day 1, following the approach in Figure 8 for August, 1996 model runs. We see a general correlation between the two altitudes, with a linear correlation coefficient of 0.57: with 51 data points this correlation is significant at the 95% level. Again, such a correlation would be expected if the gravity waves were refracted at ~ 40 km to propagate more vertically into the mesosphere. When data from the NCEP analyses from June are included in model runs, the linear correlation coefficient increases to ~ 0.64 . This correlation is poorer than for 1996 model experiments (Figure 8), suggesting more oblique wave propagation from 40 km to 80 km during 2001.

[52] Figure 16 plots gravity wave activity at 40 km as a function of experiment day based on model runs using analysis and forecast data. The black curve results from running the GROGRAT model with the AVN analyses, and is smoothed using a three day running mean and offset vertically by +0.12 (as in Figure 13). Each successively lighter curve shows model output based on AVN forecast data: the lightest line is output using +4-day AVN forecasts, the next darker line is the prediction based on the +3-day forecast fields, and so on. One can see that, although all the curves have very similar time variations, the model runs using AVN forecast data systematically predict more gravity wave activity than runs using later forecasts and analysis. This was observed during the actual forecasting experiment, and is still not well understood. It suggests greater transmission and/or greater amplitude

growth of model-generated waves using long-range forecast fields compared to shorter-range forecast and analysis fields.

6. General Discussions

[53] Based on lidar data and ray-based gravity wave modeling during August 1996 and summer 2001, we found reasonable correspondences between model and data. The only variables that were allowed to change in the gravity wave model runs were background atmospheric conditions, specifically the winds, temperatures, and geopotential heights in the troposphere and lower stratosphere. Variable wave filtering/refraction of waves due to background variations led to model-generated variations in wave activity (Figures 5, 13 and 16). These model findings support results reported by *Eckermann* [1992] and *Alexander* [1996, 1998] that a model with invariant sources but realistic variations in background winds can replicate specific aspects of stratospheric gravity wave observations. However, these results differ from those earlier studies in that the invariant source spectrum was derived from observations using backtracing and constrained to this geographic region. Only then did model results agree reasonably with lidar observations during summer. One would suspect that if this same source spectrum was used for model experiments during winter, the model results would not match observations.

[54] Correspondences between modeled and measured gravity wave activity, along with the correlation between the modeled gravity wave fields at 40 km and 80 km, supports theories presented in *GKT98* and *Gerrard et al.* [2002a, 2004] of correlations and physical connections between upper stratospheric gravity wave activity and mesospheric clouds measured over Sondrestrom. As discussed by *Thayer et al.* [2003], the presence of gravity waves in a MC model enabled them to better match modeled MC characteristics with MCs observed with the

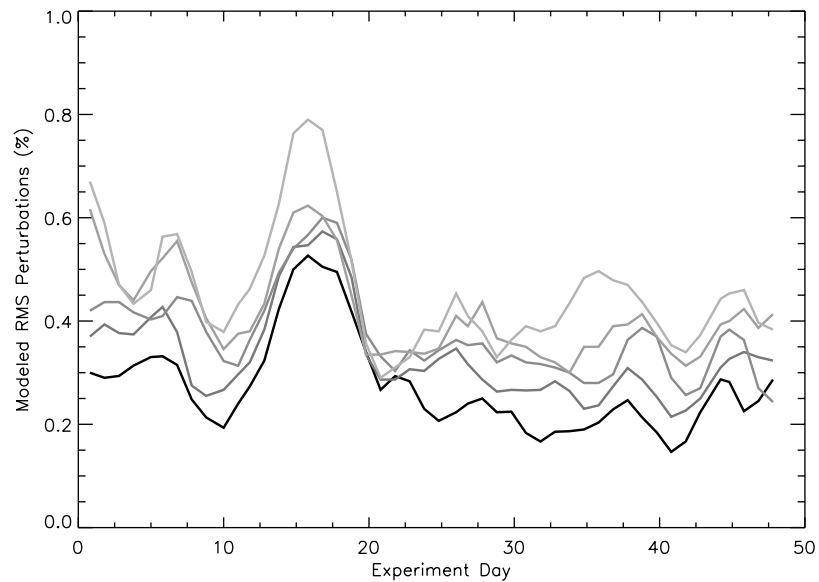


Figure 16. Comparison of gravity wave activity from the ray-tracing model experiments using AVN analyses and forecasts during summer, 2001. The black line represents ray-traced gravity wave activity computed from the AVN background analyses. These data are smoothed by a three day running mean and offset vertically by +0.12. Each successively lighter line is a forecast prediction of gravity wave activity at 40 km based on AVN forecasts, plotted in the same manner as the black analysis line, and offset by one day. Hence, the lightest line is the prediction from the model run using NCEP 4-day forecast fields. The *x* axis is in experiment days, with day 1 corresponding to July 5th, 2001.

lidar. Eliminating waves produced MCs that were generally thicker and brighter than those observed. Our modeling provides additional support for the MC sublimation hypothesis through gravity wave influence, discussed by *Jensen and Thomas* [1994] and *Rapp et al.* [2002].

[55] The most problematic aspect of these ray model experiments concerns the selection of a representative tropospheric gravity wave source spectrum. We initially suspected that a more realistic source spectrum could be derived by backtracing gravity waves from 40 km to 6 km for each individual day in August 1996. Another approach we considered specifies a geographically uniform spectrum of gravity waves at each grid point and lets these waves propagate upwards, allowing the atmosphere to naturally filter out unrealistic waves [e.g., *Eckermann, 1992; Alexander, 1998*]. We tested both approaches and found the processing time to be too computationally expensive to be practical in a forecasting mode for 2001. Additionally, gravity wave activity was over-predicted in these model runs, ultimately masking any clear daily variability. For example, when a uniform gravity wave source spectrum was launched at each grid point, the modeling results “washed-out” any daily gravity wave variability due to the large number of unrealistic gravity wave “sources.” We note that the choices of source spectra and the way multiray output is averaged to yield a final activity measurement can be done in many different ways in ray-tracing models, and some metrics compare better with certain observations than others [e.g., *Eckermann, 1992; Alexander, 1998*].

[56] The tropospheric gravity wave source spectrum used in this study, which is based solely on August 5th, 1996 backtracing results, could be interpreted as artificially tuning our results to reproduce 1996 observations. As such,

these ray model experiments using this source spectrum simulate the potential for similar gravity wave activity as on August 5th, 1996 to reach the stratosphere and mesosphere over Sondrestrom. Since this particular tropospheric gravity wave source spectrum produces model results broadly consistent with observations during 1996, it may represent a reasonable first-order approximation of the true source spectrum for this specific region at this specific time period. The large uncertainties in extratropical nonorographic gravity wave sources [*Fritts and Alexander, 2003*] make it infeasible at present to specify these sources deterministically, as is done with some specific tropical deep convective sources [e.g., *Alexander, 1996*] or with orographic gravity waves in winter [e.g., *Bacmeister, 1993; Bacmeister et al., 1994*]. Thus, model inversion experiments constrained by observations seem to be the best way we have at present to crudely estimate tropospheric sources for linear models: indeed, this same general approach was used in a somewhat different context by *Alexander and Rosenlof* [2003] to infer data-constrained wave source parameters for gravity wave drag parameterizations in global models.

7. Conclusions

[57] We have conducted ray model experiments in and around Sondrestrom, Greenland using background atmospheres specified at lower heights by NCEP analyses during August, 1996 and NCEP AVN analyses and forecasts during summer 2001, and at upper heights (where NCEP data abate) by CIRA-86 atmospheric values. We used a tropospheric source that was derived by backtracing an observationally-constrained spectrum of waves at 40 km to 6 km on August 5, 1996. The model-generated wave activity from

these runs was compared to upper stratospheric gravity wave activity measured with the molecular/aerosol lidar at Sondrestrom. The comparisons between model output and observations were reasonable for the runs in August, 1996 (Figure 5) and more variable for the analysis/forecast runs in 2001. We compared modeled gravity wave activity at 40 km to gravity wave activity at 80 km and delineated a statistically significant correlation between the two fields. This supports experimental findings reported by GKT98, Gerrard et al. [2002a, 2004], and Thayer et al. [2003] that the gravity wave activity measured by molecular lidar at 40 km over Sondrestrom influences MC variability observed by aerosol lidar in the mesosphere over Sondrestrom.

[58] However, it is difficult to state conclusively how well the model runs using NCEP forecast fields during 2001 (presented in Section 5) replicate experimentally observed gravity wave activity in the upper stratosphere. Though the general trends throughout the summer period are consistent, missing data during key periods prevent more definitive tests.

[59] Possible future research involving the methods outlined in this paper could focus on some of the following issues: development of a more comprehensive/realistic tropospheric source spectrum, analysis of the saturation mechanisms of the middle atmospheric gravity waves, use of more realistic mesospheric winds/temperatures (if/when available), extension of model runs and data analysis to the regions around the Arctic Lidar Observatory for Middle Atmospheric Research (ALOMAR) facility in northern Norway (69°N, 16°E), and extension of the analysis to winter intervals in an attempt to better understand the influence of the polar vortex on gravity wave activity suggested in Gerrard et al. [2002b].

[60] **Acknowledgments.** The authors of this paper would like to thank the members of the Sondrestrom research facility for their contributions to this paper. We also would like to thank the Scientific Computing Division of the National Center for Atmospheric Research for data and computer support. TJK was supported in part by the NSF grant ATM 00-86385, and JPT was supported by the NSF Cooperative Agreement ATM-9813556. SDE was supported partially by NASA's Geospace Sciences Program (NRA-00-01-SRT-115:R3572).

References

- Alexander, M. J. (1996), A simulated spectrum of convectively generated gravity waves: Propagation from the tropopause to the mesopause and the effects on the middle atmosphere, *J. Geophys. Res.*, *101*, 1571–1588.
- Alexander, M. J. (1998), Interpretations of observed climatological patterns in stratospheric gravity wave variance, *J. Geophys. Res.*, *103*, 8627–8640.
- Alexander, M. J., and K. H. Rosenlof (2003), Gravity-wave forcing in the stratosphere: Observational constraints from the Upper Atmosphere Research Satellite and implications for parameterization in global models, *J. Geophys. Res.*, *108*(D19), 4597, doi:10.1029/2003JD003373.
- Bacmeister, J. T. (1993), Mountain-wave drag in the stratosphere and mesosphere inferred from observed winds and a simple mountain-wave parameterization scheme, *J. Atmos. Sci.*, *50*, 377–399.
- Bacmeister, J. T., P. A. Newman, B. L. Gary, and K. R. Chan (1994), An algorithm for forecasting mountain wave related turbulence in the stratosphere, *Wea. Forecasting*, *9*, 241–253.
- Dewan, E. M., and R. E. Good (1986), Saturation and the 'universal' spectrum for vertical profiles of horizontal scalar winds in the atmosphere, *J. Geophys. Res.*, *91*, 2742–2748.
- Dörnbrack, A., and M. Leutbecher (2001), Relevance of mountain wave cooling for the formation of polar stratospheric clouds over Scandinavia: A 20 year climatology, *J. Geophys. Res.*, *106*, 1583–1593.
- Dörnbrack, A., M. Leutbecher, H. Volkert, and M. Wirth (1998), Mesoscale forecasts of stratospheric mountain waves, *Meteorol. Appl.*, *5*, 117–126.
- Dörnbrack, A., M. Leutbecher, J. Reichardt, A. Behrendt, K.-P. Müller, and G. Baumgarten (2001), Relevance of mountain wave cooling for the formation of polar stratospheric clouds over Scandinavia: Mesoscale dynamics and observations for January 1997, *J. Geophys. Res.*, *106*, 1569–1581.
- Eckermann, S. D. (1992), Ray-tracing simulation of the global propagation of inertia gravity waves through the zonally-averaged middle atmosphere, *J. Geophys. Res.*, *97*, 15,849–15,866.
- Eckermann, S. D., and C. J. Marks (1997), GROGRAT: A new model of the global propagation and dissipation of atmospheric gravity waves, *Adv. Space Res.*, *20*, 1253–1256.
- Eckermann, S. D., and P. Preusse (1999), Global measurements of stratospheric mountain waves from space, *Science*, *286*, 1534–1537.
- Fleming, E. L., S. Chandra, J. J. Barnett, and M. Corney (1990), Zonal mean temperature, pressure, zonal wind, and geopotential height as functions of latitude, *Adv. Space Res.*, *10*(12), 11–59.
- Fritts, D. C., and M. J. Alexander (2003), Gravity wave dynamics and effects in the middle atmosphere, *Rev. Geophys.*, *41*(1), 1003, doi:10.1029/2001RG000106.
- Fritts, D. C., and P. K. Rastogi (1985), Convective and dynamical instabilities due to gravity wave motions in the lower and middle atmosphere: Theory and observations, *Radio Sci.*, *20*(4), 1247–1277.
- Fritts, D. C., J. R. Isler, and G. E. Thomas (1993), Wave breaking signatures in noctilucent clouds, *Geophys. Res. Lett.*, *20*, 2039–2042.
- Gerrard, A. J., T. J. Kane, and J. P. Thayer (1998), Noctilucent clouds and wave dynamics: Observations at Sondrestrom, Greenland, *Geophys. Res. Lett.*, *25*, 2817–2820.
- Gerrard, A. J., T. J. Kane, J. P. Thayer (2000), Year-round temperature and wave variance measurements of the Arctic middle atmosphere for 1995–1998, *Atmospheric Science Across the Stratopause*, edited by D. E. Siskind, S. D. Eckermann, and M. E. Summers, *Geophys. Monogr. Ser.* 123, AGU, Washington, D. C.
- Gerrard, A. J., J. P. Thayer, and T. J. Kane (2002a), Mesospheric clouds and the duality of gravity waves, *EOS Trans AGU*, *83*(43), Fall Meet. Suppl., Abstract 488.
- Gerrard, A. J., T. J. Kane, J. P. Thayer, T. J. Duck, J. A. Whiteway, and J. Fiedler (2002b), Synoptic-scale study of the Arctic polar vortex's influence on the middle atmosphere: I. Observations, *J. Geophys. Res.*, *107*(D16), 4276, doi:10.1029/2001JD000681.
- Gerrard, A. J., T. J. Kane, J. P. Thayer, and S. D. Eckermann (2004), Concerning the upper stratospheric gravity wave and mesospheric cloud relationship over Sondrestrom, Greenland, *J. Atmos. Solar-Terr. Phys.*, *66*(3–4), doi:10.1016/j.jastp.2003.12.005.
- Hagan, M. E., and J. M. Forbes (2002), Migrating and nonmigrating diurnal tides in the middle and upper atmosphere excited by tropospheric latent heat release, *J. Geophys. Res.*, *107*(D24), 4754, doi:10.1029/2001JD001236.
- Hagan, M. E., and J. M. Forbes (2003), Migrating and nonmigrating semi-diurnal tides in the upper atmosphere excited by tropospheric latent heat release, *J. Geophys. Res.*, *108*(A2), 1062, doi:10.1029/2002JA009466.
- Hedin, A. E. (1991), Extension of the MSIS thermosphere model into the middle and lower atmosphere, *J. Geophys. Res.*, *96*, 1159–1172.
- Hertzog, A., F. Vial, A. Dörnbrack, S. D. Eckermann, B. M. Knudsen, and J.-P. Pommereau (2002), In-situ observations of gravity waves and comparisons with numerical simulations during the SOLVE/THESEO 2000 campaign, *J. Geophys. Res.*, *107*(D20), 8292, doi:10.1029/2001JD001025.
- Hiscox, A. L., A. J. Gerrard, T. J. Kane (2001), Atmospheric Wave Propagation: Modeling and Results Associated with Maui-MALT, *AMOS Technical Conference*, Maui, HI.
- Holton, J. R., and M. J. Alexander (2000), The role of waves in the transport circulation of the middle atmosphere, *Atmospheric Science Across the Stratopause*, edited by D. E. Siskind, S. D. Eckermann, and M. E. Summers, *Geophys. Monogr. Ser.* 123, AGU, Washington, D. C.
- Horinouchi, T., T. Nakamura, and J. Kosaka (2002), Convectively generated mesoscale gravity waves simulated throughout the middle atmosphere, *Geophys. Res. Lett.*, *29*(21), 2007, doi:10.1029/2002GL016069.
- Hurrell, J. W., Y. Kushnir, G. Ottersen, and M. Visbeck (2003), An Overview of the North Atlantic Oscillation, in *The North Atlantic Oscillation*, edited by J. W. Hurrell et al., *Geophys. Monogr. Ser.* 134, AGU.
- Jensen, E. J., and G. E. Thomas (1994), Numerical simulations of the effects of gravity waves on noctilucent clouds, *J. Geophys. Res.*, *99*, 3421–3430.
- Kim, Y.-J., S. D. Eckermann, and H.-Y. Chun (2003), A overview of the past, present and future of gravity-wave drag parameterization for numerical climate and weather prediction models, *Atmos. Ocean*, *41*, 65–98.
- Kishore, P., S. P. Namboothiri, K. Igarashi, Y. Murayama, R. A. Vincent, A. Dowdy, D. J. Murphy, and B. J. Watkins (2003), Further evidence of hemispheric differences in the MLT mean wind climatology: Simultaneous MF radar observations at Poker Flat (65°N, 147°W) and Davis

- (69°S, 78°E), *Geophys. Res. Lett.*, *30*(6), 1336, doi:10.1029/2002GL016750.
- Labitzke, K. G., and H. van Loon (1999), *The Stratosphere: Phenomena, History, and Relevance*, 179 pp., Springer-Verlag, New York.
- Lübken, F.-J. (1999), Thermal structure of the Arctic summer mesosphere, *J. Geophys. Res.*, *104*, 9135–9149.
- Marks, C. J., and S. D. Eckermann (1995), A three dimensional nonhydrostatic ray-tracing model for gravity waves: Formulation and preliminary results for the middle atmosphere, *J. Atmos. Sci.*, *52*, 1959–1984.
- Pawson, S., and B. Naujokat (1997), Trends in daily wintertime temperatures in the northern stratosphere, *Geophys. Res. Lett.*, *24*, 575–578.
- Pawson, S., et al. (2000), The GCM-Reality Intercomparison Project for SPARC (GRIPS): Scientific issues and initial results, *Bull. Am. Meteorol. Soc.*, *81*, 781–796.
- Pierce, R. B., et al. (2003), Large-scale chemical evolution of the Arctic vortex during the 1999/2000 winter: HALOE/POAM III Lagrangian photochemical modeling for the SAGE III-Ozone Loss and Validation Experiment (SOLVE) campaign, *J. Geophys. Res.*, *108*(D5), 8317, doi:10.1029/2001JD001063.
- Pitteway, M. L. V., and C. O. Hines (1963), The viscous damping of atmospheric gravity waves, *Can. J. Phys.*, *41*, 1935–1948.
- Preusse, P., A. Dörnbrack, S. D. Eckermann, M. Riese, B. Schaeler, J. T. Bacmeister, D. Broutman, and K. U. Grossmann (2002), Space-based measurements of stratospheric mountain waves by CRISTA, 1, Sensitivity, analysis method, and a case study, *J. Geophys. Res.*, *107*(D23), 8178, doi:10.1029/2001JD000699.
- Randel, W. J. (1987), The evaluation of winds from geopotential height data in the stratosphere, *J. Atmos. Sci.*, *44*, 3097–3120.
- Rapp, M., F.-J. Lübken, A. Müllemann, G. E. Thomas, and E. J. Jensen (2002), Small scale temperature variations in the vicinity of NLC: Experimental and model results, *J. Geophys. Res.*, *107*(D19), 4392, doi:10.1029/2001JD001241.
- Senft, D. C., and C. S. Gardner (1991), Seasonal variability of gravity wave activity and spectra in the mesopause region at Urbana, *J. Geophys. Res.*, *96*, 17,229–17,264.
- Siskind, D. E., S. D. Eckermann, J. P. McCormack, M. J. Alexander, and J. T. Bacmeister (2003), Hemispheric differences in the temperature of the summertime stratosphere and mesosphere, *J. Geophys. Res.*, *108*(D2), 4051, doi:10.1029/2002JD002095.
- Tan, K. A., and S. D. Eckermann (2000), Numerical model simulations of mountain waves in the middle atmosphere over the southern Andes, *Atmospheric Science Across the Stratopause*, edited by D. E. Siskind, S. D. Eckermann, and M. E. Summers, *Geophys. Monogr. Ser.* 123, AGU, Washington, D. C.
- Thayer, J. P., N. Nielsen, and J. Jacobsen (1995), Noctilucent cloud observations over Greenland by a Rayleigh Lidar, *Geophys. Res. Lett.*, *22*, 2961–2964.
- Thayer, J. P., N. B. Nielson, R. E. Warren, C. J. Heinselman, and J. Sohn (1997), Rayleigh Lidar system for middle atmosphere research in the Arctic, *Opt. Eng.*, *36*, 2045–2061.
- Thayer, J. P., M. Rapp, A. J. Gerrard, E. Gudmundsson, and T. J. Kane (2003), Gravity wave influences on Arctic mesospheric clouds as determined by a Rayleigh lidar at Sondrestrom, Greenland, *J. Geophys. Res.*, *108*(D8), 8449, doi:10.1029/2002JD002363.
- Thomas, L., A. K. P. Marsh, D. P. Wareing, and M. A. Hassan (1994), Lidar observations of ice crystals associated with noctilucent clouds at middle latitudes, *Geophys. Res. Lett.*, *21*, 385–388.
- von Cossart, G., P. Hoffmann, U. von Zahn, P. Kechut, and A. Hauchecorne (1996), Mid-latitude noctilucent cloud observations by lidar, *Geophys. Res. Lett.*, *23*, 2919–2922.
- Weinstock, J. (1990), Saturated and unsaturated spectra of gravity waves and scale dependent diffusion, *J. Atmos. Sci.*, *47*, 2211–2225.
- Wickwar, V. B., M. J. Taylor, J. P. Herron, and B. A. Martineau (2002), Visual and lidar observations of noctilucent clouds above Logan, Utah, at 41.7°N, *J. Geophys. Res.*, *107*(D7), 4054, doi:10.1029/2001JD001180.
- Zhu, X. (1993), Radiative damping revisited: Parameterization of damping rate in the middle atmosphere, *J. Atmos. Sci.*, *50*, 3008–3021.

S. D. Eckermann, Middle Atmospheric Dynamics Section, Code 7646, E. O. Hulburt Center for Space Research, Naval Research Laboratory, Washington, DC 20375-5352, USA. (stephen.eckermann@nrl.navy.mil)

A. J. Gerrard, Kinard Laboratory, Clemson University, Clemson, SC 29634, USA. (agerrar@clemson.edu)

T. J. Kane, Pennsylvania State University, 121 Electrical Engineering East, University Park, PA 16802, USA. (tjk7@psu.edu)

J. P. Thayer, Ionospheric and Space Physics Group, SRI International, 333 Ravenswood Avenue, Menlo Park, CA 94025, USA. (thayer@sri.com)

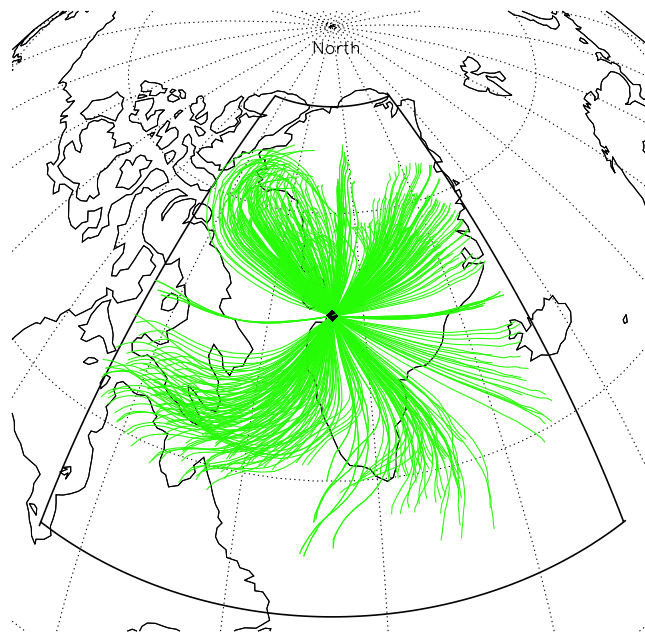


Figure 3. Backtraced (reverse ray traced) group trajectories of the gravity wave spectrum in Figure 2 on August 5th, 1996 (12 UT). Only gravity waves that stayed within the model domain (in dark black lines) and made it to 6 km are plotted. Dark diamonds represent initial location of each gravity wave (all located above Sondrestrom at 40 km altitude in this case). Latitude-longitude gridlines are spaced every 15° .

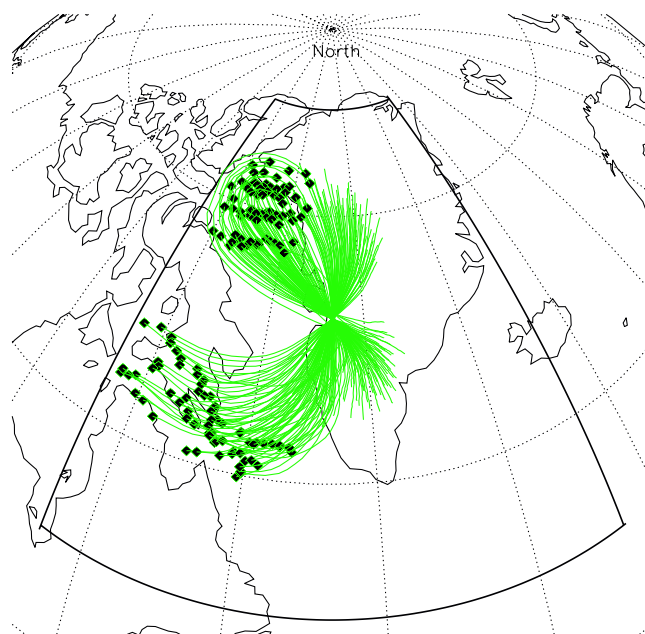


Figure 4. Gravity wave ray group trajectories initiated with the tropospheric spectrum obtained at 6 km from Figure 3 on August 5th, 1996. As expected, all rays converge to a single point over Sondrestrom at 40 km. The waves were then allowed to propagate further in altitude/time, and only gravity waves that reached 80 km and satisfied observability criteria are plotted. Dark diamonds represent the initial location of each gravity wave in the troposphere. Latitude-longitude gridlines are spaced every 15° .

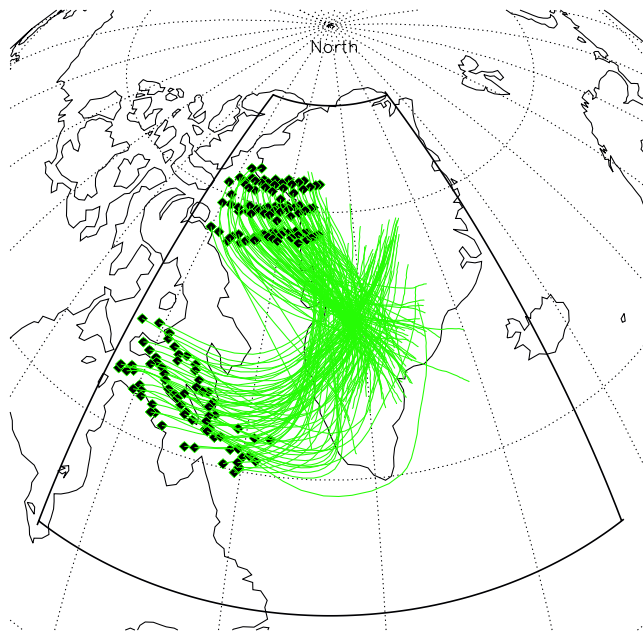


Figure 6. Gravity wave ray group trajectories initiated at 6 km with the tropospheric spectrum obtained from Figure 3 on August 6th, 1996. Only gravity waves that met the 80 km observability criteria are plotted. Dark diamonds represent the initial location of each gravity wave in the troposphere. Latitude-longitude gridlines are spaced every 15°.

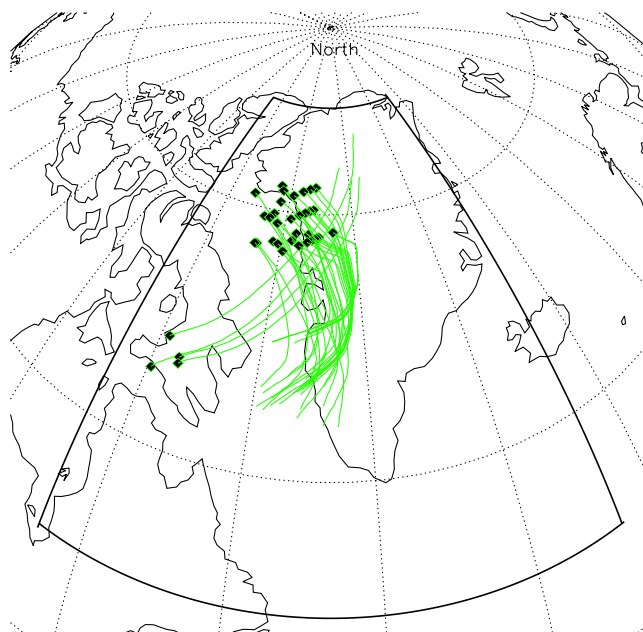


Figure 7. Gravity wave ray group trajectories initiated at 6 km with the tropospheric spectrum obtained from Figure 3 on August 11th, 1996. Only gravity waves that met the 80 km observability criteria are plotted. Dark diamonds represent the initial location of each gravity wave in the troposphere. Latitude-longitude gridlines are spaced every 15°.

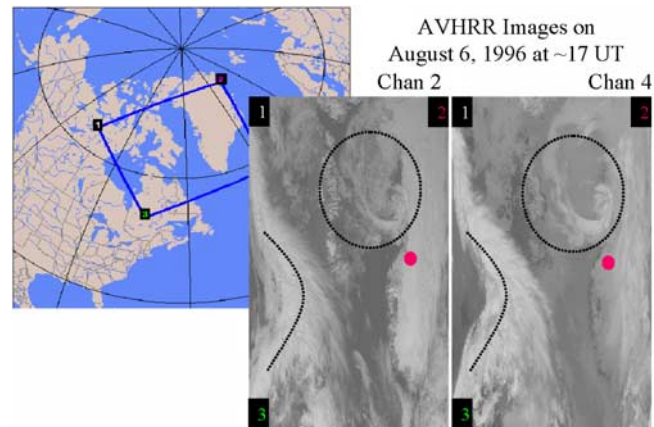


Figure 11. Data from AVHRR channels 2 (visible-near infrared) and 4 (far infrared) on August 6th, 1996 at ~17 UT. For ease of orientation, the numbering on the map corresponds to the numbering on the images. The Greenland ice shelf and the coast are visible on the right in these images.

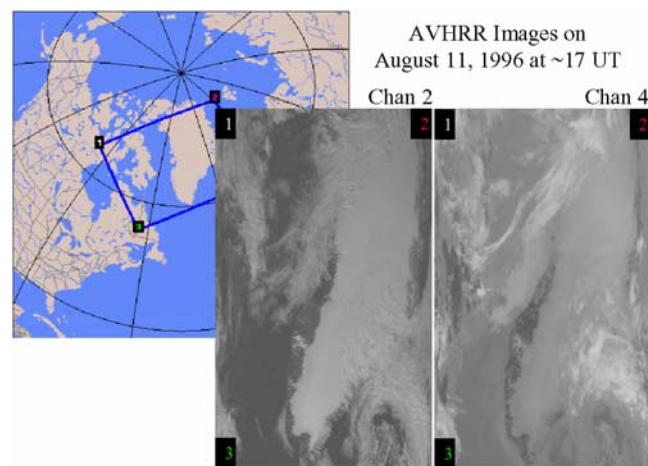


Figure 12. Data from AVHRR channels 2 (visible-near infrared) and 4 (far infrared) on August 11th, 1996 at ~17 UT. For ease of orientation, the numbering on the map corresponds to the numbering on the images. The Greenland ice shelf and the coast are visible on the right in these images.

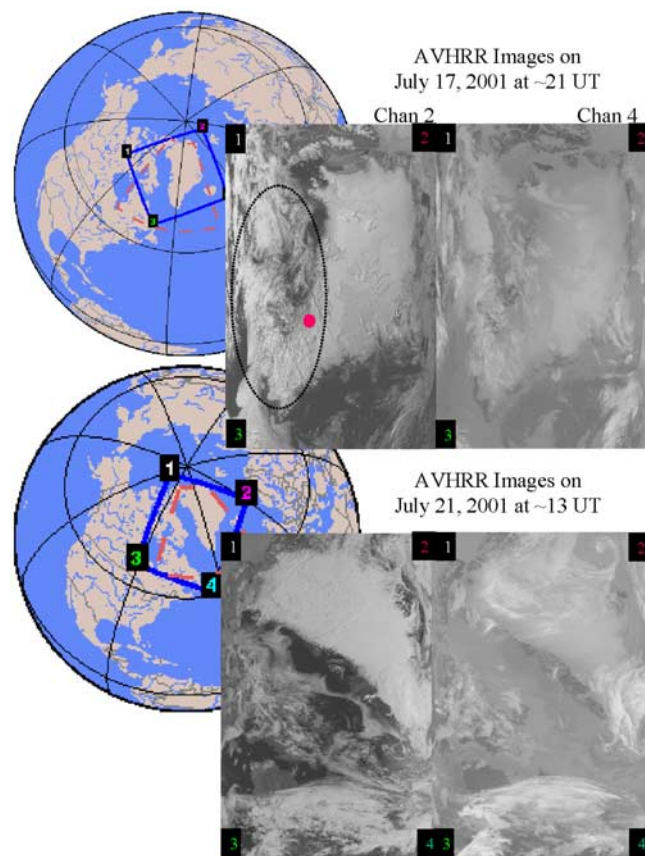


Figure 14. Data from AVHRR channels 2 (visible-near infrared) and 4 (far infrared) on experiment day 13 and day 17 (July 17th and July 21st of 2001, respectively) at ~21 UT. For ease of orientation, the numbering on the map corresponds to the numbering on the images. The Greenland ice shelf and the coast are visible on the top-right in these images. The dashed red line represents the model boundary. These data are representative of similar data observed during this period.